# An Energy Autonomous 400 MHz Active Wireless SAW Temperature Sensor Powered by Vibration Energy Harvesting

Zhu, Yao; Zheng, Yuanjin; Gao, Yuan; Made, Darmayuda I.; Sun, Chengliang; Je, Minkyu; Gu, Alex Yuandong

# An Energy Autonomous 400 MHz Active Wireless SAW Temperature Sensor Powered by Vibration Energy Harvesting

Yao Zhu, *Student Member, IEEE*, Yuanjin Zheng, *Member, IEEE*, Yuan Gao, *Member, IEEE*, Darmayuda I Made, Chengliang Sun, Minkyu Je, *Senior Member, IEEE*, and Alex Yuandong Gu

*Abstract*— **An energy autonomous active wireless surface acoustic wave (SAW) temperature sensor system is presented in this paper. The proposed system adopts direct temperature to frequency conversion using a Lithium Niobate SAW resonator for both temperature sensing and high-Q resonator core in a cross-coupled RF oscillator. This arrangement simplifies the temperature sensor readout circuit design and reduces the overall system power consumption. A power conditioning circuit based on buck–boost converter is utilized to provide high efficiency power extraction from piezoelectric energy harvester (PEH) and dynamic system power control. The SAW resonator is fabricated in-house using a two-step lithography procedure while the RF oscillator as well as the PEH power conditioning circuit are implemented in standard 65-nm and 0.18-µm CMOS processes respectively. The measured RF transmitter output power is -15 dBm with a phase noise of -99.4 dBc/Hz at 1 kHz offset, achieving a figure of merit (FOM) of -217.6 dB. The measured temperature sensing accuracy is ±0.6 °C in -40 °C to 120 °C range. Fully powered by a vibration PEH, the proposed energy autonomous system has a self-startup voltage of 0.7 V and consumes an average power of 61.5 µW.**

*Index Terms*—**SAW, temperature sensor, wireless, low power, vibration energy harvest, energy autonomous, power management, SAW oscillator.**

## I. INTRODUCTION

SURFACE acoustic wave (SAW) device has been widely used in temperature sensing for its merits of wide temperature sensing range, passive sensing capability and natural compatibility with wireless systems. In passive wireless SAW temperature sensors [1-7], the received signal is processed in acoustic domain by delay, correlation, or filtering function, etc, and then transmitted out by the same antenna through backscattering. Although passive wireless SAW sensor has the advantages of simple structure and batteryless operation, it has major drawbacks such as short communication distance, low tolerance to interferences and mismatches, and strict requirement on the frequency and timing of the interrogation signal [5, 6]. To overcome these issues, active wireless SAW temperature sensors have been developed [8, 9] to boost output power to extend the communication range. However, due to the usage of the active circuits, system life time becomes a critical issue which is dependent on circuit power consumption and system battery capacity. For applications in harsh environment or remote/inaccessible area, battery replacement is not always feasible. Therefore, sensor systems which can utilize ambient energy harvesting, to achieve long-term self-sustaining operation are preferred.

A typical energy autonomous wireless temperature sensor comprises of three major building blocks: an energy harvesting unit, a temperature sensor with its readout circuit and a RF transmitter. The energy harvester circuits extract power from different types of energy sources such as solar [10], near field coupling [11], RF [12] and vibration [13] to power the system. The sensor readout circuit converts the temperature information into analog or digital signal. Then the data is modulated on the carrier signal by RF modulator and transmitted out by the transmitter.

In this paper, ambient vibration energy is harvested to power a wireless temperature sensor node, targeting environmental and structural monitoring applications such as monitoring of manufacture and assembly equipment, household appliances, civil infrastructure, HVAC (heating, ventilation and air conditioning), etc. The temperature sensor readout circuit and the RF modulator are merged into one circuit block. This is acheived by adopting the SAW resonator as both the temperature sensing element and the high quality factor (Q-factor) resonator core of the RF oscillator for direct temperature to frequency conversion. The major system design challenge is to accumulate the harvested energy efficiently to power the temperature sensor and RF transmitter in a duty cycled manner. This is because the peak power consumption of RF transmitter is approximately 1 mW to support long range wireless data communication. However, the harvested power

may goes down to µW level, depending on the ambient vibration strength. Therefore, the system needs to dynamically control the duty cycle according to the harvested power level.

To achieve dynamic system power control, a high efficiency energy harvester power management circuit is designed in this work. In addition to the piezoelectric transducer interface circuits demonstrated in [20], a power management module including an on-chip low dropout voltage regulator (LDO) and undervoltage-lockout (UVLO) circuits have been integrated on chip to provide energy accumulation and undervoltage shut down function to enable energy autonomous operation under different input power level. The entire system is able to self startup with a minimum 0.7 V input voltage and consumes an average power of 61.5 µW.

This paper is organized as follows. System architecture is presented in Section II. The SAW resonator design and modeling are presented in Section III. The details of the individual circuit blocks, such as the oscillator and energy harvester power conditioning circuit are presented in Section IV. Section V reports the measurement results and section VI concludes the paper.

## II.  SYSTEM ARCHITECTURE

Fig. 1 shows the overall system block diagram of the proposed active wireless SAW temperature sensor, including a piezoelectric energy harvester (PEH) power conditioning circuit and a SAW-based RF transmitter. The power conditioning circuit consists of a switch-based negative voltage converter (NVC), a non-inverting buck-boost converter, a 3-stage current starving ring oscillator and a LDO. After the NVC rectifies the incoming AC signal, the buck-boost converter synthesizes a resistive input impedance for maximum energy extraction and voltage boosting [20]. All the timing signals in the buck-boost converter are generated by the ring oscillator. The LDO regulates the storage energy and provides a stable voltage supply to the SAW-based RF transmitter. A cross-coupled SAW-based RF oscillator with driving amplifier is used as the RF transmitter. This SAW resonator serves as both the temperature sensing element and the high-Q resonant tank of the RF oscillator. The temperature dependent RF signal generated by the oscillator is transmitted out through an antenna.

Direct temperature to frequency conversion reduces the system complexity and saves power. In addition, it eliminates the inaccuracy which could come from the temperature dependent modulation of the output RF frequency [15, 16]. Self-startup and smart power management are the other two major functions in the system. To illustrate the system self startup principle, Fig. 2 shows the transient waveforms at the key nodes in the system. During the cold start-up period, the system starts with the passive charging since all the active circuits are OFF. Once the voltage $V_{bb}$ on the storage capacitor $C_s$ is high enough to drive the ring oscillator, the buck-boost converter is activated and the system switches to higher efficiency active charging mode. When $V_{bb}$ surpasses a predetermined threshold voltage $V_H$, the LDO is enabled to
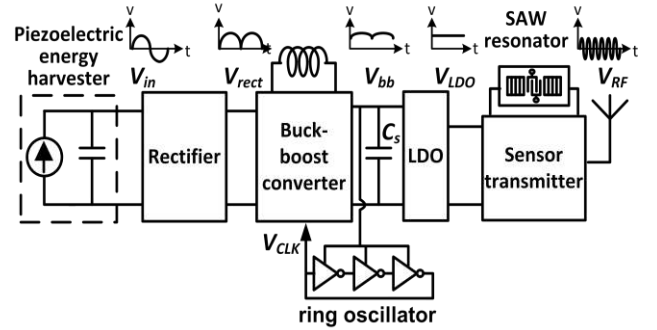


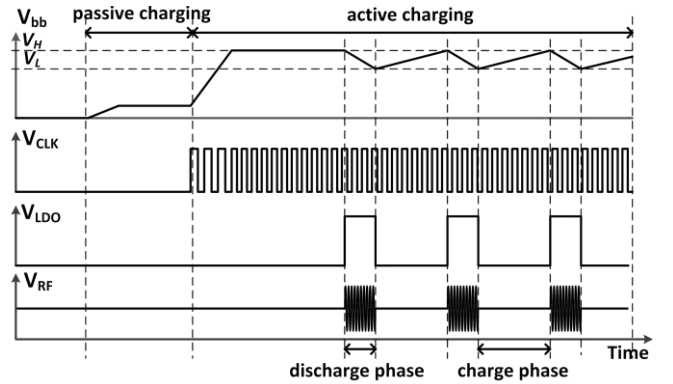Figure 1. Block diagram of the proposed energy-autonomous wireless SAW temperature sensor.



Figure 2. Timing diagram of the proposed system.
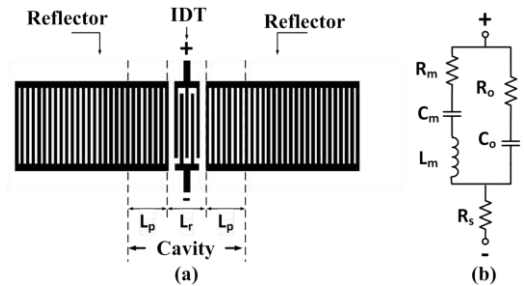


Figure 3. (a) The conceptual view of the schematic, and (b) the equivalent circuit of the one-port SAW resonator.

provide the regulated power supply to the SAW sensor transmitter. With the discharge of $C_s$, when $V_{bb}$ drops below another threshold voltage $V_L$, the LDO will shut down and the system goes to charging phase again to accumulate energy. This function ensures that the system can support transmitter with higher pulsed output power for longer communication distance even under weak ambient vibration.

## III.  SAW RESONATOR

Instead of the commonly used SAW delay line structure, a one-port SAW resonator based temperature sensor is adopted in this work to achieve high Q-factor and low power consumption. In the one-port SAW resonator with the geometric structure as shown in Fig. 3(a), the acoustic waves are excited by the inter-digital transducer (IDT) and constructively reflected by the reflectors at the resonant frequency, $f_o$, to form standing waves. $f_o$ is determined by the SAW velocity $v_{SAW}$ and the reflector pitch $L_R$, given by $f_o = v_{SAW} / 2L_R$. Thus the temperature coefficient of frequency (TCF) of the resonator is derived as:

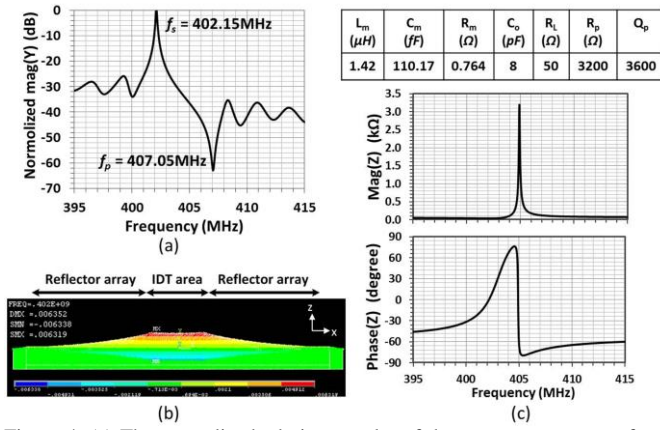Figure 4. (a) The normalized admittance plot of the resonator response from the two-dimensional ANSYS FEM simulation. (b) The contour plot of the SAW displacement in ANSYS Y-direction of the resonator at simulated series resonant frequency 402.15 MHz. (c) The derived parameters in the equivalent circuit model based on ANSYS simulation and the plot of the resonator impedance over frequency.

$$TCF = \frac{\partial f_o / \partial T}{f_o} = \frac{\partial v_{SAW}}{v_{SAW} \partial T} - \frac{\partial L_R}{L_R \partial T} \qquad (1)$$

where $T$ is the ambient temperature. 128° YX Lithium Niobate (LiNbO$_3$) is chosen as the substrate material because of its high coupling coefficient which makes the design of low loss SAW resonator feasible. In addition, the linear and high temperature coefficient of $v_{SAW}$ at around 75 ppm/°C [17] over a wide temperature range makes it well suited for temperature sensing. Fig. 3(b) shows the equivalent circuit of the one-port SAW resonator. $C_o$ represents the static capacitance of the IDT and $R_L$ is the resistance of the IDT finger and routing traces. $L_m$, $C_m$ and $R_m$ describe the resonator behavior at frequencies close to the resonant frequency. There are two resonant frequencies in the one-port SAW resonators, namely series resonant frequency $f_s$ where the impedance of resonator is lowest and parallel resonant frequency $f_p$ where the resonator has the highest impedance value. The impedances of the resonator at $f_s$ and $f_p$ are as follows:

$$f_s = \frac{1}{2\pi\sqrt{L_m C_m}} \text{ and } R_s = R_m + R_L, \qquad (2)$$

$$f_p = f_s\sqrt{1 + \frac{C_m}{C_o}} \text{ and } R_p = \frac{L_m}{R_m(C_m + C_o)} + R_L. \qquad (3)$$

To simulate the device, a three-dimensional (3D) full structural model would best represent the physical phenomena that occur during SAW device operation. However, considering that the device length for a resonator will be hundreds of wavelengths, the number of elements required for the entire device structure (IDTs and reflectors) using finite element modeling (FEM) will be sizeable. A full model would hence require substantial processor and memory to obtain a complete solution. Some researchers made use of the periodic boundary condition to reduce the SAW structure to only one or several finger pairs [23, 24], which substantially reduced the model

size. However, it can only be applied to the semi-infinite periodic structure to do a rough estimation of the mode shapes and the natural resonant frequencies.

In this work, we reduce the size of the model to a more manageable level without losing the simulation accuracy by making a few valid approximations. The first of which is a reduction to two dimensions (2D). SAWs are straight-crested waves whose particle motions are localized in the sagittal plane (xz plane). The waves do not hold much important information as one traverse in the y-direction and hence the entire characteristics can be described by a 2D model. A second approximation is the model depth. The penetration depth into the substrate of SAWs is known to be small with particle displacements declining to less than 5% of surface values within 2 to 3 wavelengths beneath the surface [25]. This allows a model representing only 5 to 8 wavelengths of device depth to be built without loss in solution accuracy.

The 2D finite element method (FEM) simulation is performed using commercial software ANSYS in both frequency and time domain to optimize the performance of SAW resonator, especially on the enhancement of the impedance level and quality factor at $f_p$. The pitch of both the reflector ($L_R$) and IDT finger is 4.8 μm with 50% metal line-width to pitch ratio. The simulated series resonant frequency is 402.15 MHz as shown in Fig. 4(a). It can be observed from the SAW displacement in ANSYS z-direction as shown in Fig. 4(b) that the SAW reflector arrays constructively reflect majority of the SAW at the series resonant frequency and confines most of the SAW energy in the IDT area.

To facilitate the design of the sensor circuit and estimation of the sensor power consumption, the initial values of the SAW equivalent circuit parameters are extracted from the FEM simulation following the method described in [18]. Taking the losses due to substrate dissipation, air damping, etc. into consideration, a damping factor $\alpha = 5 \times 10^{-4}$ [19] is included to extract the two key parameters: reflector array reflection coefficient $|\Gamma|$ and effective cavity length $L_{eff}$ as derived in equation (4-5). $|\Gamma|$ is the fraction of SAW reflected by the reflector array comprising of $N_r$ number of reflector lines, each with a reflectivity $r$ at resonant frequency. $L_{eff}$ is defined by the location $L_p$ from the edge of the reflector where the long enough reflector array can be replaced by a single narrow band mirror:

$$|\Gamma| = \left(1 - \frac{\alpha}{r}\right)\left(1 - (1-r)^{N_r}\right), \qquad (4)$$

$$L_{eff} = \frac{1}{1 + \frac{\alpha}{r}}\left(2L_p + L_{rr}\right) \qquad (5)$$

where $L_{rr}$ is the distance between the two reflector array edges.

The equivalent circuit parameters can be calculated using the following expressions:

$$C_o = N_t C_s, \qquad (6)$$

$$Z = -\left(\frac{2}{gm} + \frac{1}{j\omega C_{hp}}\right)$$
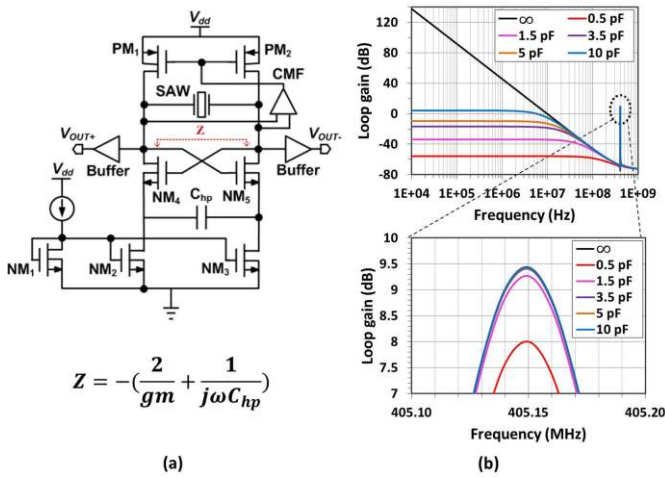
(a)                                (b)

Figure 5. (a) The simplified schematic of the SAW sensor based differential oscillator circuit. (b) The loop gain of the oscillator over frequency with sweeping $C_{hp}$.
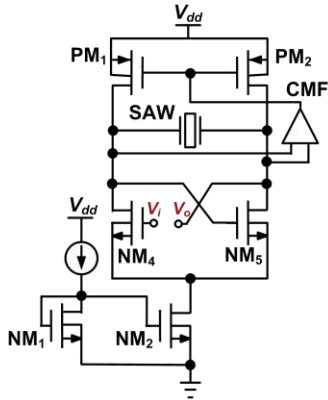


Figure 6. The schematic for DC loop gain analysis of the conventional cross-coupled oscillator with SAW resonator tank.

$$R_t = \frac{1}{8N_t^2 k^2 f_o C_s}, \tag{7}$$

$$L_m = \frac{R_o L_{eff}}{4|\Gamma| f_o}, \tag{8}$$

$$C_m = \frac{1}{\omega_o^2 L_m}, \tag{9}$$

$$R_m = \frac{1 - |\Gamma|}{2|\Gamma|} R_o \tag{10}$$

where $N_t$ is the number of IDT finger pairs, $C_s$ is the capacitance per IDT finger pair and $k^2$ is the coupling coefficient.

Minimizing the system power consumption and ensuring the temperature sensing accuracy are the two main considerations when designing the SAW temperature sensor. The current consumption of the oscillator is inversely proportional to the resonance impedance level of the resonator. To increase $R_p$ at the parallel resonant frequency $f_p$, the one port resonator can be designed to have less number of IDT finger pairs to reduce the static capacitance $C_o$. However, the resonator with smaller $C_o$ is more sensitive to the capacitive loading from the oscillator circuit and packaging parasitics, which could result in reduced loaded quality factor $Q_L$ as well as smaller equivalent $R_p$.

Moreover, the frequency pulling by the external capacitance will be more significant which could deteriorate the temperature accuracy of the system. To maintain high $R_p$ and minimize the frequency pulling at the same time, the resonator is designed to have 20 pairs of IDT fingers with theoretical $C_o$ of 8 pF. The sensor resonant frequency is designed in 400 MHz frequency band with the in air wavelength at around one meter which enables the RF signals to diffract around large obstructions.

By introducing the metal resistance and substrate loss and using the modeling method described above, the derived SAW resonator equivalent circuit parameters and impedance plot are shown in Fig. 4(c). The quality factor is 3600 at the parallel resonance frequency 407.05 MHz, with $R_p$ of 3.2 kΩ. These parameters will be later referenced when designing the sensor circuit.

## IV. CIRCUIT BLOCKS

### A. RF oscillator

The schematic of SAW oscillator is shown in Fig. 5(a). The SAW resonator serves as the resonance tank in the oscillator, thus the oscillation frequency will be determined by the resonant frequency of the SAW resonator. Since the SAW resonant frequency is linearly proportional to the ambient temperature, a direct temperature to RF frequency conversion can be achieved. A differential topology is adopted for better supply and ground noise rejection. Cross-coupled oscillator architecture is chosen as it requires less current to start up and provide higher output swing to meet the stringent power budget of the energy autonomous system. A differential common-mode feedback circuit is used to fix the DC drain voltages of $NM_4$ and $NM_5$. Unlike LC tank resonator, the SAW resonator has high impedance at low frequency due to the presence of static capacitance $C_o$. If the conventional cross-coupled oscillator structure is adopted, the lack of DC path will make the oscillator prone to latch up (positive feedback of DC) rather than oscillate. The open loop gain of a conventional cross-coupled oscillator circuit with SAW resonator tank as shown in Fig. 6 is derived as below.

$$\frac{V_o}{V_i} = g_{m\_n4}\left[\frac{1}{j\omega C_{gs\_n5}} \parallel r_{ds\_p1} \parallel \left(Z_{SAW} + r_{ds\_p2} \parallel r_{ds\_n5}\right)\right] \tag{11}$$

where $g_{m\_n4}$ is the transconductance of $NM_4$, $C_{gs\_n5}$ is the gate to source capacitance of $NM_5$, $Z_{SAW}$ is the impedance resonator, and $r_{ds}$ is drain-to-source resistance of the transistor. At DC, the resonator is capacitive, thus the impedances of $Z_{SAW}$ and $C_{gs\_n5}$ are infinite and only the output resistances of the transistors are still present in (11). The output resistances of the transistors are designed to be much larger than $Z_{SAW}$ at the desired oscillation frequency to minimize the loading to the tank. Hence the voltage gain at DC is always higher than that at $f_o$ ($0.5g_{m\_n4}Z_{SAW}$). Without any high pass filter applied to the voltage gain, the oscillator will oscillator at close to DC instead of at the resonant frequency of the SAW sensor.
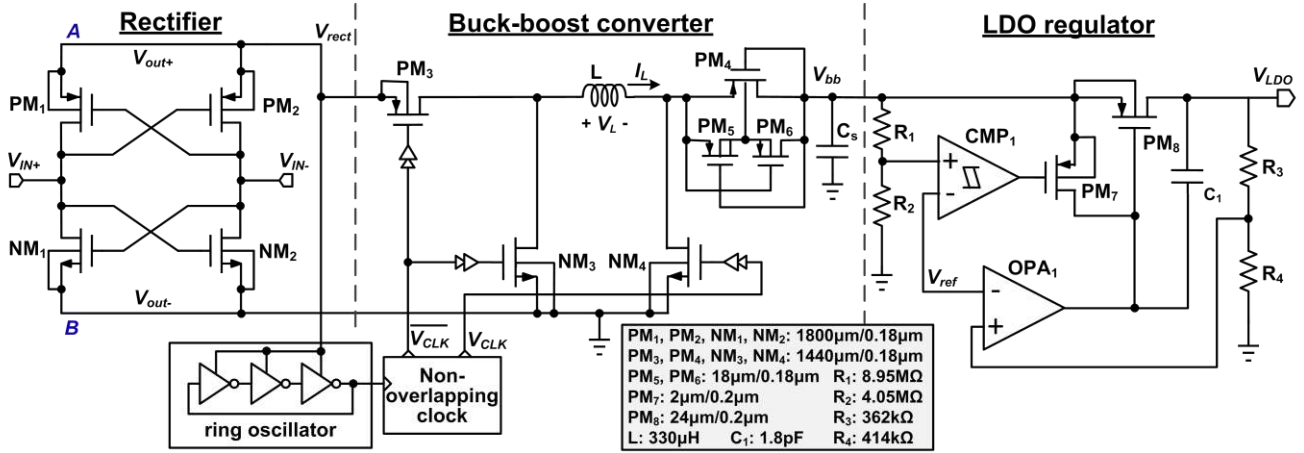
Figure 7. The energy harvester circuits.

Therefore, to resolve this issue, the differential branches are supplied with individual current sources and a capacitor $C_{hp}$ is included to perform the high pass filtering to the loop gain as shown in Fig. 5(a). To analyze the loop gain of the circuit, small signal analysis is performed. The impedance looking into the drain terminals of $NM_4$ and $NM_5$ is:

$$Z_{drain} = -\left(\frac{2}{g_m} + \frac{1}{j\omega C_{hp}}\right) \quad (12)$$

where $g_m$ is the transcondutance of the transistor $NM_4$ and $NM_5$, and $\omega$ is the angular frequency. It can be observed from (12) that the equivalent transconductance $G_m = -1/Z_{drain}$ of the oscillator is brought down at low frequency by $C_{hp}$.

The oscillation is sustained when the following conditions are fulfilled:

$$|A_{CL}| = 1 \text{ and } \angle A_{CL} = 0°. \quad (13)$$

Assuming that the impedance looking into the PMOS loads is much higher than that of the tank impedance at oscillation frequency, the loop gain $A_{CL} = G_m Z_{SAW}$ of the oscillator when $g_m = 1$ mS is plotted in Fig. 5(b) to illustrate the effect of $C_{hp}$, where $Z_{SAW}$ is the impedance of the SAW resonator. When $C_{hp}$ is infinite or of big value, $|A_{CL}|$ is higher than 0 dB at low frequency which could cause parasitic oscillation. With the decrease of $C_{hp}$, the low-frequency gain is greatly suppressed, with the compromise of $|A_{CL}|$ degradation at the desired oscillation frequency. Therefore, to avoid the low frequency spurious oscillation yet maintaining the relatively high loop gain at RF frequency, $C_{hp}$ is chosen as 3.5 pF which gives 25 dB out of band suppression and less than 0.1 dB gain reduction at the desired oscillation frequency. To achieve high $|A_{CL}|$, the width over length $W/L$ ratio of transistors can be made large to obtain higher $g_m$. The penalty is that increasing the capacitive loading from the larger MOS transistor will pull down the sensor impedance, and in turn degrade the $|A_{CL}|$ of the oscillator. Taken these trade-offs into consideration, $NM_4$ and $NM_5$ are sized to be 80μm/60nm. The simulation using the SAW resonator equivalent circuit parameters derived in section III

shows that the minimum startup current drawn by oscillator core and common mode feedback circuits is 120 μA under 1 V voltage supply. A common source amplifier is used to drive the 50 Ω antenna and isolate the oscillator core from the load to minimize the frequency pulling effect.

### B. Energy Harvester Circuits

Fig. 7 shows the schematic of the energy harvester circuit. The NVC employs a cross-coupled switching transistor architecture which reduces the conduction forward voltage drop to $2V_{ds}$ [20]. During the positive half cycle, with PMOS transistor $PM_1$ and NMOS transistor $NM_2$ turning on, current flows from A to the output via $PM_1$ and returns to B via $NM_2$. During the negative half cycle, $PM_2$ and $NM_1$ turn on, so current flows from B to the output via $PM_2$ and return to A via $NM_1$. PMOS body and NMOS body are tied to $V_{out+}$ and $V_{out-}$ respectively without any need of dynamic bulk regulation. $V_{out+}$ is connected to next stage for further processing while $V_{out-}$ is used as the system ground reference point. A discontinuous conduction mode (DCM) buck-boost converter behaves like a lossless impedance converter [21]. By tuning its parameters, suboptimal impedance matching for energy extraction can be synthesized regardless of the variation in loading condition. Instead of four MOS switches [22], only three MOS switches are used in this buck-boost converter design and a passive diode connected MOS provides the reverse current blocking for DCM operation. A 3-stage current starving ring oscillator together with a divide-by-2 divider generates the 1 MHz clock with 25% duty cycle. Duty cycling based on clock division has little dependence on process and voltage variation. This also provides a tighter control on synthesized resistive input impedance for wide power supply range. A non-overlapping clock (NOC) block generates the control signals to drive the MOS switches, which is used to control the power MOSFET switching without shoot-through current.

An on-chip LDO consisting of a pass transistor $PM_8$ and an error amplifier $OPA_1$ is used to provide stable power supply for the RF transmitter. To avoid the drainage of $C_s$ during the energy accumulation period, an UVLO circuit is designed with a hysteresis comparator $CMP_1$ as shown in Fig. 7. During the normal operation, $CMP_1$ compares $V_{bb}$ with a threshold voltage $V_{ref}(R_1+R_2)/R_2$, generated by the on-chip bandgap reference.
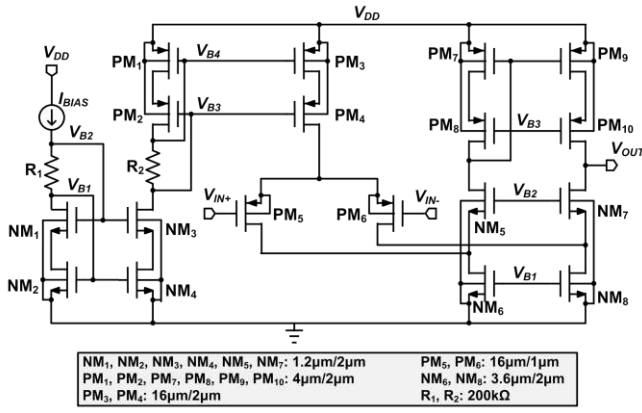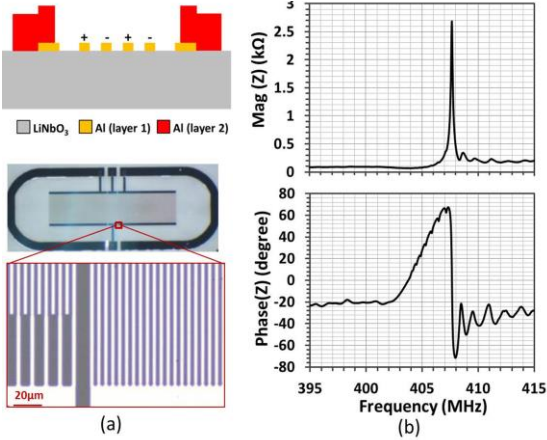
Figure 8. The schematic of the error amplifier OPA$_1$.

NM$_1$, NM$_2$, NM$_3$, NM$_4$, NM$_5$, NM$_7$: 1.2μm/2μm
PM$_1$, PM$_2$, PM$_7$, PM$_8$, PM$_9$, PM$_{10}$: 4μm/2μm
PM$_3$, PM$_4$: 16μm/2μm
PM$_5$, PM$_6$: 16μm/1μm
NM$_6$, NM$_8$: 3.6μm/2μm
R$_1$, R$_2$: 200kΩ



Figure 9. (a) The cross-section schematic and the microphoto of the SAW sensor. (b) The measured SAW sensor impedance at room temperature.

Two threshold voltages $V_L$ and $V_H$ are generated by CMP$_1$. When $V_{bb} < V_L$ (1.2 V), CMP1 output is LOW to turn on PM$_7$, so the source and gate of PM$_8$ are shorted to disable PM$_8$. When $V_{bb} > V_H$ (1.3 V), the CMP$_1$ output is HIGH, PM$_7$ is shut down and LDO is activated to power up the RF oscillator. The schematic of the LDO error amplifier OPA$_1$ is shown in Fig. 8. When PM$_7$ is ON, there is a leakage current flow through the output stage of OPA$_1$. However, because of the high output impedance of the cascode configuration used in the output stage, the leakage current is limited to less than 1 μA.

## V. MEASUREMENT RESULTS

### A. SAW Resonator

The SAW resonator is in-house fabricated using a two-step photolithography procedure to pattern the aluminum (Al) onto the 128° YX LiNbO$_3$ substrate. The cross-section view and the microphoto of the SAW resonator are shown in Fig. 9(a). The first Al layer with 80 nm thickness defines the IDT and reflector array patterns and the second Al layer with 500 nm thickness is for contact pads. The metal line width and spacing of the reflector and IDT are both 2.4 μm. The measured magnitude and phase of the resonator impedance at room temperature is plotted in Fig. 9 (b). The parallel resonance $f_p$ happens at 407.6 MHz, with $R_p$ of 2685 Ω and Q-factor of 2950. The slight frequency and impedance level shift compared with the FEM
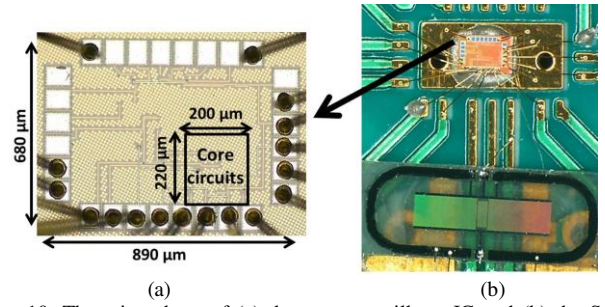


Figure 10. The microphoto of (a) the sensor oscillator IC and (b) the SAW sensor and the oscillator IC which are wire bonded on the PCB.
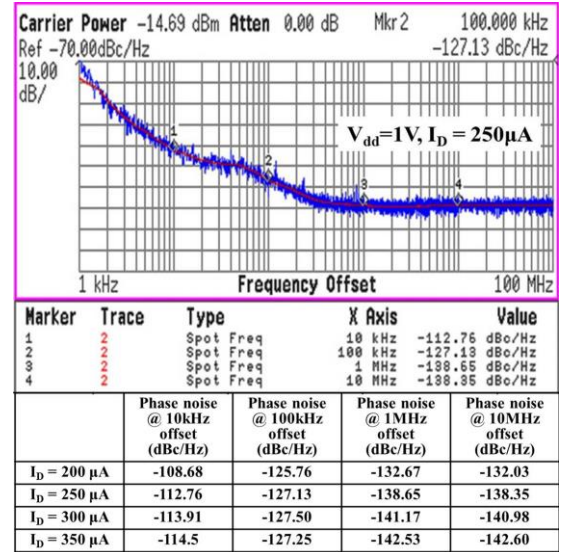


| | Phase noise @ 10kHz offset (dBc/Hz) | Phase noise @ 100kHz offset (dBc/Hz) | Phase noise @ 1MHz offset (dBc/Hz) | Phase noise @ 10MHz offset (dBc/Hz) |
|---|---|---|---|---|
| I$_D$ = 200 μA | -108.68 | -125.76 | -132.67 | -132.03 |
| I$_D$ = 250 μA | -112.76 | -127.13 | -138.65 | -138.35 |
| I$_D$ = 300 μA | -113.91 | -127.50 | -141.17 | -140.98 |
| I$_D$ = 350 μA | -114.5 | -127.25 | -142.53 | -142.60 |

Figure 11. The measured phase noise of the SAW sensor oscillator under different bias conditions.

simulation results is due to the variation of the piezoelectric material property as well as the fabrication tolerances.

### B. RF Oscillator

The RF oscillator circuit has been implemented in a standard 65-nm CMOS process from Global Foundries. The circuit and the SAW sensor chips are both wire bonded to the Rogers 4350B printed circuit board (PCB) for testing as shown in Fig. 10. Oscillation starts up when the core circuits including the cross-coupled SAW oscillator and the common mode feedback circuits consume 150 μA under voltage supply as low as 0.7 V. The low startup voltage and current allow the sensor to meet the limited power budge given by the vibration energy harvester in a range of truly energy autonomous sensor systems. The phase noise at 1 kHz and 10 kHz offset from carrier frequency of 407.2 MHz is measured to be -99.39 dBc/Hz and -113.01 dBc/Hz as shown in Fig. 11, with the figure-of-merit (FOM) of -217.6 dB and -211.2 dB respectively, when the sensor oscillator is biased with DC current of 250 μA from 1 V supply. The oscillator FOM is calculated from the equation below [26][27]:

$$FOM = L(\Delta\omega) - 20\log\left(\frac{\omega_o}{\Delta\omega}\right) + 10\log\left(\frac{P_{diss}}{1mW}\right) \quad (13)$$
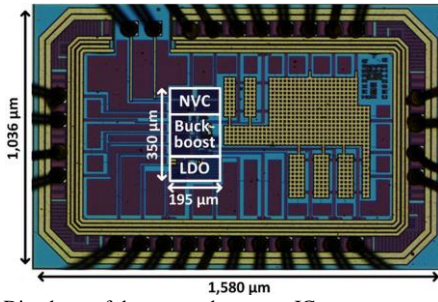
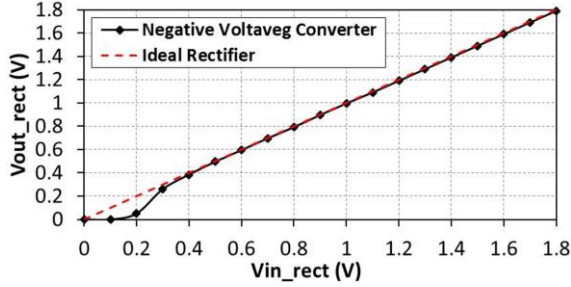Figure 12. Die photo of the energy harvester IC.


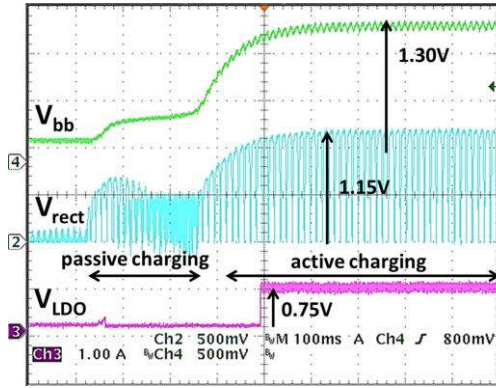
Figure 13. Measure input and output voltage of the NVC.



Figure 14. The startup waveforms of the energy harvest circuit.

where $L(\Delta\omega)$ is the phase noise at the specified offset, $\omega_o$ is the oscillation frequency, $\Delta\omega$ is the frequency offset from the carrier, and $P_{diss}$ is the DC power consumed by the oscillator core circuits. The phase noise performance of the oscillator under different bias conditions at room temperature is summarized in Fig. 11.

### C.  Energy Harvester

The proposed circuit has been implemented in a standard 0.18-μm CMOS process from Global Foundries. Fig. 12 shows the chip micrograph. A commercial PEH (Volture V21BL) mounted on a mechanical shaker is used to characterize the performance of the circuit. The measured output versus input voltage curve of the NVC is as shown in Fig. 13 indicating a power efficiency of 98% for input voltage as small as 500 mV. The buck-boost converter achieves a power efficiency of 60% when the input power is in the range of 60 μW to 130 μW. Consuming 11 μA, the LDO regulator outputs a stable voltage with the level adjusted by the voltage divider.

The measured self startup waveforms of energy harvester circuits are shown in Fig. 14. At the beginning, the ring oscillator is not powered up, hence the buck-boost converter works in the passive charging mode. Once the buck-boost



① Temperature chamber  ② Shaker control  ③ Oscilloscope  ④Spectrum analyzer
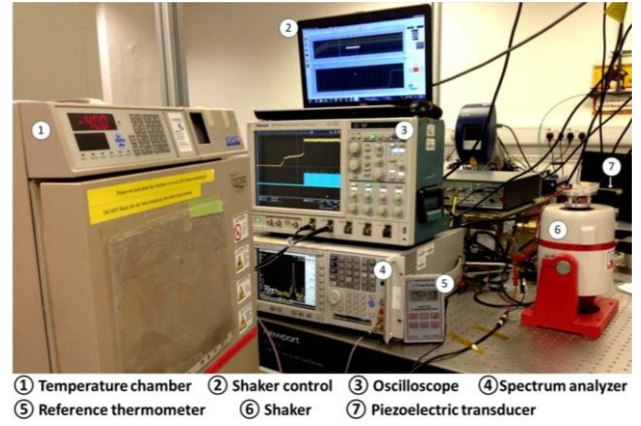⑤ Reference thermometer  ⑥ Shaker  ⑦ Piezoelectric transducer

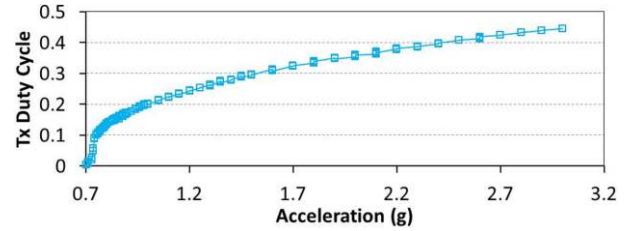Figure 15. The system level measurement setup.



Figure 16. The sensor transmitter duty cycle under different vibration strength.

converter output voltage exceeds 0.7 V, the ring oscillator starts to oscillate with a gradually increased output frequency. It kicks start the converter and suboptimal impedance matching is attained. During the passive charging phase, the buck-boost converter tracks the rectifier output. At the active charging phase, as shown in Fig. 14, the converter boosts the RMS voltage of the rectifier output from 0.8 V to 1.3 V and activates the LDO.

### D.  System

The system level measurement setup is captured in Fig. 15. The PEH is mounted on shaker (LDS V406), whose acceleration is controlled by a laptop. The energy harvesting and sensor transmitter circuits are placed inside the temperature chamber (ESPEC SU-240), with the intermediate testing points and transmitter output connecting to the oscilloscope (Tektronix DPO 7354) and the spectrum analyzer (Agilent E4448A), respectively.

In order to meet the power budget and maximize the sensor output power simultaneously, the sensor node duty cycling is deployed under the control of the power management unit. When the capacitor $C_s$ at the boost/buck-boost converter outputs charges to $V_H = 1.3$ V, the LDO is activated and provides stable supply voltage to the RF transmitter. The duty cycle of the LDO and sensor transmitter under different vibration strength is plotted in Fig. 16. Once the acceleration experienced by the PEH reaches 0.7 g, the system is able to self startup and fully supported by energy harvesting. The transmitter ON time is increased with the increase of acceleration. At 0.7 g of acceleration, the LDO and the sensor transmitter has a duty cycle of 3.2% (LDO and transmitter on-time $t_{on} = 400$ μs and off-time $t_{off} = 12.1$ ms as shown in Fig. 17). During the transmitter ON period, the sensor transmitter

TABLE II. COMPARISON WITH PRIOR ART

| | [10] | [11] | [12] | [13] | This work |
|---|---|---|---|---|---|
| Temperature sensor | BJT | Resistive | CMOS | Capacitive | SAW resonator |
| Circuit technology | 0.35-μm CMOS | 0.18-μm CMOS | 0.13-μm CMOS | 0.13-μm CMOS | 0.18-μm/65-nm CMOS |
| Energy source | Solar/RF | Inductive link | RF | Vibration | Vibration |
| Temperature range | -20°C - 120°C | 25°C - 42°C | -40°C - 125°C | 50°C - 230°C | -40°C - 120°C |
| Temperature accuracy | 1°C | ±0.09°C | NA | 0.36°C | ±0.6°C |
| Power consumption | 942.9μW (normal) 226.3μW (alarm) | 53μW (average) Duty cycle: NA | 8.55 to 14.4mW (Tx) 2.7μW(sensor) | 30μW (average) Duty cycle: 0.2% | 61.5μW (average) Duty cycle: 3.2% |
| Tx frequency | 403MHz | 868MHz | 2.1GHz | 2.6GHz | 407MHz |
| Output power | -18dBm | NA | -6.4 to 5.4dBm | -0.315dBm | -15dBm |
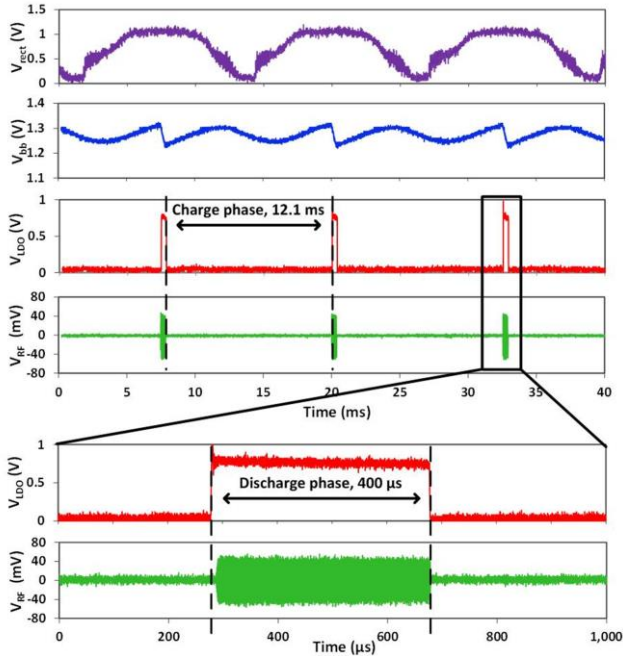


Figure 17. Measured time domain waveforms of the power management circuits and the output of the sensor which are fully powered by the vibration piezoelectric energy harvester.
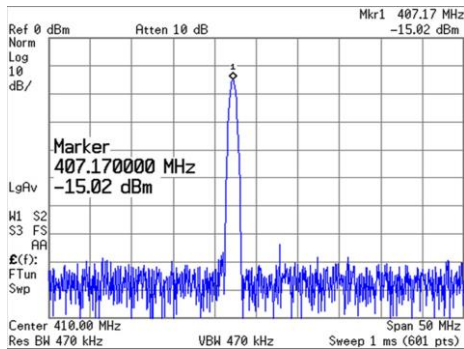


Figure 18. Measured spectrum of the energy-autonomous sensor output.

output power (to 50 Ω load) is measured to be -15 dBm as shown in Fig. 18. $V_{bb}$ is decreased as the the power drawn by the sensor node discharges $C_s$. When $V_{bb}$ drops to 1.2 V after 400 μs, the LDO is deactivated and the system enters charging phase. The peak power drawn by the sensor node and the energy harvester circuit including LDO is 1.1 mW and 39.3 μW respectively. The NVC and buck-boost converter is always *ON* with an efficiency of around 60%, while the LDO and the sensor transmitter has a duty cycle of 3.2%, thus the average power consumption of the system is calculated to be 61.5 μW. To demonstrate the wireless transmission capability of the system, a 50 Ω antenna working at 407 MHz is directly
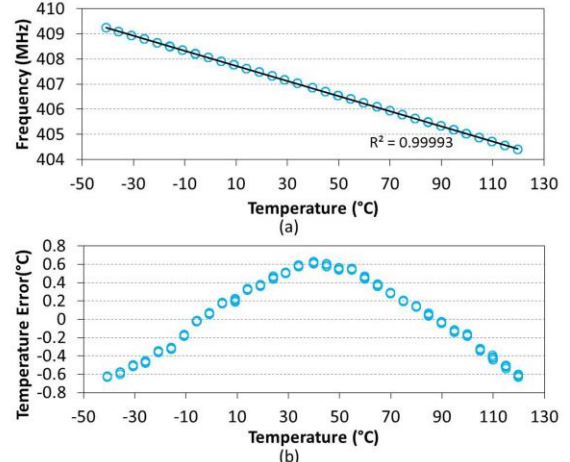


Figure 19. Experiment on temperature sensing of the sensor node. (a) The temperature dependency of the sensor output frequency in -40°C to 120°C. $R^2$ is the coefficient of determination which measures the trendline fitting quality. (b) The temperature detection errors versus temperature change.

TABLE I. SYSTEM PERFORMANCE SUMMARY

| | |
|---|---|
| Sensor type and material | SAW one-port resonator on 128° YX LiNbO₃ |
| Circuit technology | 0.18-μm/65-nm CMOS |
| Temperature accuracy | ±0.6 °C |
| Temperature range | -40 °C to 120 °C |
| Temperature sensitivity of frequency | -74 ppm /°C |
| Average power consumption | 61.5 μW |
| Output power | -15 dBm |
| Transmission frequency | 407 MHz |

connected to the sensor transmitter output. The power picked by the receiving antenna placed at two meters away is measured to be -60 dBm, which corresponds to a communication distance up to 128 meters using a narrowband receiver with -96 dBm sensitivity, by assuming every 6 dB loss per doubling the distance.

The temperature characteristics of the sensor node output is measured from -40 °C to 120 °C with a commercial digital thermometer as reference. The measured output frequency versus temperature is plotted in Fig. 19(a). The fitted frequency response has a slope of around -30 kHz/°C, which is equivalent to TCF of -74 ppm/°C. Taking the linear fitting line as the desired temperature-frequency response, the sensor inaccuracy as plotted in Fig. 19(b) is obtained by subtracting the linear fitting line from the measurement data. The figure shows that the sensor achieves a temperature accuracy of ±0.6 °C at the transmitter side. The key features of the system is summarized in TABLE I.

TABLE II compares this work with other state-of-art energy-autonomous wireless temperature sensors. To our best

knowledge, this work is the first implementation of energy autonomous wireless SAW temperature sensor ASIC using vibration self start-up technique. By adopting the high-Q SAW resonator as both the temperature sensor and transmitter resonant tank, we have provided an alternative approach than [10-13] to achieve great system simplification and transmitter phase noise reduction, good temperature accuracy in a wide temperature range, which is a promising solution to the fully energy autonomous temperature sensing system.

## VI. CONCLUSION

An energy autonomous active wireless SAW temperature sensor system has been presented in this paper. Direct conversion from temperature to frequency has been achieved by a SAW resonator based sensor transmitter which is fully powered from the vibration energy extracted by the energy efficient energy harvester and power management circuits. The sensor achieves a temperature efficiency of ±0.35 °C in the range of 25 °C to 120 °C. The wireless system outputs -15 dBm power with average power consumption of 61.5 μW and a self startup voltage of 0.7 V.

## REFERENCES

[1] A. Pohl, G. Ostermayer, and F. Seifert, "Wireless sensing using oscillator circuits locked to remote high-Q SAW resonators," *IEEE Trans. Ultrason., Ferroelectr., Freq. Control,* vol. 45, no. 5, pp. 1161-1168, Sept. 1998.

[2] L. M. Reindl, and I. M. Shrena, "Wireless measurement of temperature using surface acoustic waves sensors," *IEEE Trans. Ultrason., Ferroelectr., Freq. Control,* vol. 51, no. 11, pp. 1457-1463, Nov. 2004.

[3] A. Binder, and R. Fachberger, "Wireless SAW Temperature Sensor System for High-Speed High-Voltage Motors," *IEEE Sensors J.,* vol. 11, no. 4, pp. 966-970, Apr. 2011.

[4] D. Girbau, A. Ramos, A. Lazaro, S. Rima and R. Villarino, "Passive Wireless Temperature Sensor Based on Time-Coded UWB Chipless RFID Tags," *IEEE Trans. Microw. Theory Techn.,* vol. 60, no. 11, pp. 3623-3632, Nov. 2012.

[5] L. M. Reindl, A. Pohl, G. Scholl and R. Weigel, "SAW-based radio sensor systems," *IEEE Sensors J.,* vol. 1, no. 1, pp. 69-78, Jun. 2001.

[6] W. Buff, M. Rusko, T. Vandahl, M. Goroll and F. Moller, "A differential measurement SAW device for passive remote sensoring," *in Proc. IEEE Ultrason. Symposium,* pp. 343-346, Nov. 1996.

[7] A. Pohl, "A review of wireless SAW sensors," *IEEE Trans. Ultrason., Ferroelectr., Freq. Control,* vol. 47, no. 2, pp. 317-332, Mar. 2000.

[8] I. D. Avramov, "The RF-powered surface wave sensor oscillator - a successful alternative to passive wireless sensing," *IEEE Trans. Ultrason., Ferroelectr., Freq. Control,* vol. 51, no. 9, pp. 1148-1156, Sept. 2004.

[9] M. Viens, and J. D. N. Cheeke, "Highly sensitive temperature sensor using SAW resonator oscillator," *Sens. Actuators, A,* vol. 24, no. 3, pp. 209-211, Sept. 1990.

[10] Y.-J. Huang, T.-H. Tzeng, T.-W. Lin, C.-W. Huang, P.-W. Yen, P.-H. Kuo, C.-T. Lin, and S.-S. Lu, "A Self-Powered CMOS Reconfigurable Multi-Sensor SoC for Biomedical Applications," *IEEE J. Solid-State Circuits,* vol. 49, no. 4, pp. 851-866, Apr. 2014.

[11]

[12] M. A. Ghanad, M. M. Green, and C. Dehollain, "A remotely powered implantable IC for recording mouse local temperature with ±0.09 °C accuracy," *in Proc. Solid-State Circuits Conf. (A-SSCC),* pp. 93-96, Nov. 2013.

[13] H. Reinisch, S. Gruber, H. Unterassinger, M. Wiessflecker, G. Hofer, W. Pribyl and G. Holweg, "An Electro-Magnetic Energy Harvesting System With 190 nW Idle Mode Power Consumption for a BAW Based Wireless Sensor Node," *IEEE J. Solid-State Circuits,* vol. 46, no. 7, pp. 1728-1741, Jul. 2011.

[14] J. JaeHyuk, D. F. Berdy, L. Jangjoon, D. Peroulis and J. Byunghoo, "A Wireless Condition Monitoring System Powered by a Sub-100 μW Vibration Energy Harvester," *IEEE Trans. Circuits Syst. I, Reg. Papers,* vol. 60, no. 4, pp. 1082-1093, Apr. 2013.

[15] J. Yin, J. Yi, M. K. Law, Y. Ling, M. C. Lee, K. P. Ng, B. Gao, H. C. Luong, A. Bermak, M. Chan, W.-H. Ki, C.-Y. Tsui and M. Yuen, "A System-on-Chip EPC Gen-2 Passive UHF RFID Tag With Embedded Temperature Sensor," *IEEE J. Solid-State Circuits,* vol. 45, no. 11, pp. 2404-2420, Nov. 2010.

[16] F. Kocer, and M. P. Flynn, "An RF-powered, wireless CMOS temperature sensor," *IEEE Sensors J.,* vol. 6, no. 3, pp. 557-564, 2006.

[17] Y.-C. Shih, T. Shen, and B. P. Otis, "A 2.3 μW Wireless Intraocular Pressure/Temperature Monitor," *IEEE J. Solid-State Circuits,* vol. 46, no. 11, pp. 2592-2601, Nov. 2011.

[18] C. Campbell, Surface Acoustic Wave Devices for Mobile and Wireless Communications: Academic Press, 1998.

[19] Y. Zhu, Y. Zheng, C.-L. Wong, M. Je, L. Khine, P. Kropelnicki, and T. M. Tsai, "Design of a 843MHz 35μW SAW oscillator using device and circuit co-design technique." *in Proc. IEEE Asia Pacific Conf. on Circuits and Systems (APCCAS),* pp.328-331, Dec. 2012.

[20] P. S. Cross, "Properties of Reflective Arrays for Surface Acoustic Resonators," *IEEE Trans. on Sonics and Ultrason.*, vol. 23, no. 4, pp. 255-262, Jul. 1976.

[21] D. I Made, Y. Gao, M. T. Tan, S.-J. Cheng, Y. Zheng, M. Je, and C.-H. Heng, "A Self-Powered Power Conditioning IC for Piezoelectric Energy Harvesting From Short-Duration Vibrations," *IEEE Trans. Circuits Syst. II, Exp. Briefs,* vol. 59, no. 9, pp. 578-582, Sept. 2012.

[22] E. Lefeuvre, D. Audigier, C. Richard and D. Guyomar, "Buck-Boost Converter for Sensorless Power Optimization of Piezoelectric Energy Harvester," *IEEE Trans. Power Electron.*, vol. 22, no. 5, pp. 2018-2025, Sept. 2007.

[23] B. Sahu, and G. A. Rincon-Mora, "A low voltage, dynamic, noninverting, synchronous buck-boost converter for portable applications," *IEEE Trans. Power Electron.,* vol. 19, no. 2, pp. 443-452, Mar. 2004.

[24] Y.-B. Ke, H.-L. Li and S.-T. He, "Analysis of surface acoustic wave resonators with boundary element method," in Proc. Piezoelectricity, Acoustic Waves, and Device Applications (SPAWDA) and China Symposium on Frequency Control Technology Joint Conf., pp. 42-42, Dec. 2009.

[25] M. Hofer, N. Finger, G. Kovacs, J. Schoberl, S. Zaglmayr, U. Langer and R. Lerch, "Finite-element simulation of wave propagation in periodic piezoelectric SAW structures," *IEEE Trans. Ultrason., Ferroelectr., Freq. Control*, vol. 53, no. 6, pp. 1192-1201, Jun. 2006.

[26] H. Matthews, *Surface wave filters: design, construction, and use*: Wiley, 1977.

[27] A. Mazzanti, F. Svelto, P. Andreani, "On the amplitude and phase errors of quadrature LC-tank CMOS oscillators," *IEEE J. Solid-State Circuits*, vol.41, no.6, pp.1305-1313, Jun. 2006.

[28] W. Deng, K. Okada, A. Matsuzawa, "Class-C VCO With Amplitude Feedback Loop for Robust Start-Up and Enhanced Oscillation Swing," *IEEE J. Solid-State Circuit*, vol.48, no.2, pp.429-440, Feb. 2013.

**Yao Zhu** (S'12) received the B.Eng. (First-Class Honors) in electrical and electronic engineering from Nanyang Technological University, Singapore in 2009. She is currently a Ph.D. candidate in Nanyang Technological University, Singapore. Since August 2014, she has been a research scientist in the Institute of Microelectronic*s*, A*STAR, Singapore. Her research interests include acoustic wave micro-resonator and filter design and fabrication, as well as CMOS wireless transceiver and sensor circuits and systems design.

**Yuanjin Zheng** (M'02) received the B.Eng. and M.Eng. degrees from Xi'an Jiaotong University, Xi'an, China, in 1993 and 1996, respectively, and the Ph.D. degree from the Nanyang Technological University, Singapore, in 2001. From July 1996 to April 1998, he

was with the National Key Laboratory of Optical Communication Technology, University of Electronic Science and Technology of China. In 2001, he joined the Institute of Microelectronics (IME), Agency for Science, Technology and Research (A*STAR), and had been a principle Investigator and group leader. With the IME, he has led and developed various projects like CMOS RF transceivers, baseband system-on-a-chip (SoC) for wireless systems, ultra-wideband (UWB), and low-power biomedical ICs etc. In July 2009, he joined the Nanyang Technological University, as an assistant professor and program directors. His research interests are gigahertz RFIC and SoC design, bio-sensors and imaging, and SAW/BAW/MEMS sensors. He has authored or coauthored over 150 international journal and conference papers, 15 patents filed/granted, and several book chapters.

**Yuan Gao** (S'04-M'08) received the B.Eng. and M.Eng. degrees in electrical engineering from Huazhong University of Science and Technology, Wuhan, China in 2000, 2003, respectively, and the Ph.D. degree in electrical engineering from the National University of Singapore, Singapore, in 2008.

Since 2007, he has been with Institute of Microelectronics (IME), Agency for Science, Technology and Research (A*STAR), Singapore, where he is currently a research scientist and the principal investigator of Biomedical IC group in Integrated Circuits and Systems Laboratory. His current research interests include low-power low-voltage circuit technologies for wireless and biomedical applications, energy harvesting and biosensor interface circuits design. He has authored or coauthored more than 40 peer-reviewed international journal and conference papers and has 7 patents granted or filed.

**Darmayuda I Made** received the B.Eng. degree and the M.Sc. degree in electrical and electronic engineering from Nanyang Technological University, Singapore in 2008 and 2010, respectively.

Since 2010, he has been a Research Engineer with Institute of Microelectronics, A*STAR, Singapore. His areas of interests include dc-dc converter power management and piezoelectric energy harvester ICs.
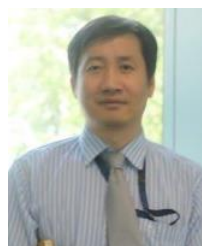
**Chengliang Sun** received the B.Sc. and Ph.D. degrees in physics from Wuhan University, Wuhan, China, in 1999 and 2006, respectively. He was a research associate, a postdoctoral associate and fellow at the Hong Kong Polytechnic University, University of Pittsburgh and then University of Wisconsin-Madison, respectively, from 2004-2011. After four years research and study in USA, he moved to Singapore in 2011. He is currently a project leader and a research scientist in the program of Sensors & Actuators Microsystems at the Institute of Microelectronics, A*Star, Singapore. His research interests include the processing and characterization of piezoelectric ceramics, polymers, and composites and their applications in sensors and actuators; micro-electromechanical systems (MEMS) and micro-fabrication; thin films for electromechanical transducer, actuator, and sensor applications. His recent research focuses on energy harvesting and thin film acoustic devices.

**Minkyu Je** (S'97-M'03-SM'12) received the M.S. and Ph.D. degrees, both in Electrical Engineering and Computer Science, from Korea Advanced Institute of Science and Technology (KAIST), Daejeon, Korea, in 1998 and 2003, respectively.

In 2003, he joined Samsung Electronics, Giheung, Korea, as a Senior Engineer and worked on multi-mode multi-band RF transceiver SoCs for cellular standards. From 2006 to 2013, he was with Institute of Microelectronics (IME), Agency for Science, Technology and Research (A*STAR), Singapore. From 2011 to 2013, he led the Integrated Circuits and Systems Laboratory at IME as a Department Head. He was also a Program Director of NeuroDevices Program under A*STAR Science and Engineering Research Council (SERC) from 2011 to 2013, and an Adjunct Assistant Professor in the Department of Electrical and Computer Engineering at National University of Singapore (NUS) from 2010 to 2013. Since 2014, he has been an Associate Professor in the Department of Information and Communication Engineering at Daegu Gyeongbuk Institute of Science & Technology (DGIST), Daegu, Korea.

His main research areas are advanced IC platform development including smart sensor interface ICs and ultra-low-power wireless communication ICs, as well as microsystem integration leveraging the IC platform for emerging applications such as intelligent miniature biomedical devices, ubiquitous wireless sensor nodes, and future mobile devices. He has more than 200 peer-reviewed international conference and journal publications. He also has more than 30 patents issued or filed.

**Alex Yuandong Gu** received his Ph.D. in Pharmaceutics and M.E.E in Electrical Engineering, both from the University of Minnesota, Twin Cities, USA in 2003.

He is the Technical Director of Miniaturised Medical Devices (MMD) and Sensors & Actuators Microsystems (SAM) programmes at the A*STAR Institute of Microelectronics (IME). He spent 10 years in the Honeywell Sensors and Wireless Lab as a principal research scientist before joining A*STAR Institute of Microelectronics. His industrial research covers broad areas include chemical and biosensors, ultrasound, chip-level thermal management, chip-level vacuum systems, and deeply miniaturized medical equipment.

He was the Principal Investigator and/or Program Manager for various externally funded research programs totaling >$15M during his 10-year tenure with Honeywell. He has authored over 20 research publications and holds more than 20 patents.